



OPEN

SUBJECT AREAS:

CHEMICAL
ENGINEERINGELECTRONIC PROPERTIES AND
DEVICES

NANOWIRES

SENSORS AND BIOSENSORS

Highly Sensitive and Multifunctional Tactile Sensor Using Free-standing ZnO/PVDF Thin Film with Graphene Electrodes for Pressure and Temperature Monitoring

James S. Lee^{1*}, Keun-Young Shin^{1*}, Oug Jae Cheong¹, Jae Hyun Kim² & Jyongsik Jang¹Received
1 August 2014Accepted
22 December 2014Published
20 January 2015Correspondence and
requests for materials
should be addressed to
J.J. (jsjang@plaza.snu.
ac.kr)* These authors
contributed equally to
this work.

¹World Class University program of Chemical Convergence for Energy & Environment, School of Chemical and Biological Engineering, Seoul National University, 151-742, Korea, ²Manufacturing Technology Team, Infra Technology Service Center, Device Business, Samsung Electronics, San #16 Banwol-Dong, Hwasung-City, Gyeonggi-Do, Korea.

We demonstrate an 80- μm -thick film (which is around 15% of the thickness of the human epidermis), which is a highly sensitive hybrid functional gauge sensor, and was fabricated from poly(vinylidene fluoride) (PVDF) and ZnO nanostructures with graphene electrodes. Using this film, we were able to simultaneously measure pressure and temperature in real time. The pressure was monitored from the change in the electrical resistance via the piezoresistance of the material, and the temperature was inferred based on the recovery time of the signal. Our thin film system enabled us to detect changes in pressure as small as 10 Pa which is pressure detection limit was 10^3 -fold lower than the minimum level required for artificial skin, and to detect temperatures in the range 20–120 °C.

Electronic skin (e-skin) mimics some of the functionality of human skin, aiming to provide sensory responses to mechanical, thermal, chemical, biological and optical stimuli. Therefore, multifunctional electronic sensors are of great interest for medical and industrial applications. In particular, thin-film systems have been investigated for use in sensor devices, due to the convenient, low-cost processing techniques and flexibility. Moreover, the development of a flexible thin-film device that can replace the epidermis has important applications in the treatment of injuries. Much effort has been devoted to enhancing the performance of pressure-sensing films. Integrated, strain-gauge sensors have been reported by Karp-Yang Shu *et al.*,¹ that could detect pressure, shear and torsion. In contrast, relatively little attention has been paid to sensing of combined external stimuli in a single device, such as sensing mechanical strain and temperature. It is not straightforward to design a system that can discriminate among different stimuli, because the fabrication of such multifunctional sensors typically involves integration of a number of organic and inorganic devices using hybrid matrix arrays and circuit elements, which involves complex, expensive processes.^{2–13} Thus, it is still challenging to realize a sensor that enable to detect multiple stimuli accurately and simultaneously.

To date, much effort has been devoted to investigating the piezoelectric and pyroelectric properties of thin films for fabrication of multifunctional sensors. The piezoelectric and pyroelectric properties of thin films enable fabrication of multifunctional sensors. Reverse-piezoelectricity can respond to an applied mechanical displacement by inducing an electric potential and pyroelectricity.^{14–19} An example of such a material is poly(vinylidene fluoride) (PVDF), which has attracted much interest as a next-generation piezoelectric and pyroelectric material because of its light weight, flexibility, low power consumption, and non-toxicity.^{20–24} We have previously demonstrated the piezoelectric effect of PVDF for application as an acoustic actuator.⁴ The enhanced permittivity, which is related to the polarization and dipole moment of PVDF, is key factor for improving the piezoelectric and pyroelectric properties of PVDF. For this reason, the semiconductor zinc oxide (ZnO) is of interest, as it may increase the piezoelectric response, is thermally stable, and may increase the permittivity of PVDF^{25,26}. Therefore, a hybrid PVDF matrix with a ZnO nanofiller may enable fabrication of a hybrid piezoelectric/pyroelectric sensor.

Furthermore, piezoresistive and pyroresistive sensing, which transduces mechanical displacement and temperature signals into an electrical signal, may be a valuable and simple monitoring method for small structures¹. In particular, a change in the electron mobility or resistance can be measured using a transistor structure.



Here we report a highly sensitive hybrid functional gauge sensor using a PVDF thin film and vertically grown ZnO nanorods. As electrodes, a graphene was utilized which is derived from the vacuum-assisted reduction of graphene oxide (GO) film by inkjet printing. To our knowledge, this is the first experimental demonstration of the detection of two different independent stimuli (i.e., pressure and temperature) simultaneously and in real time. The pressure was inferred from the change in the electrical resistance via the piezo-resistance of the material, and the temperature was determined based on the recovery time of the signal. The morphology of the ZnO nanostructures was controlled to maximize the response of the device, and the output signals were monitored while controlling the pressure and temperature to calibrate the device.

Results

Fabrication of a PVDF- and ZnO-based sensor. Fig. 1a and b show a schematic diagram and photograph of the flexible multilayer device. A large areal density of ZnO nanorods was embedded in the PVDF on a reduced graphene oxide (rGO)-treated flexible polyethylene terephthalate (PET) thin film. First, exfoliated GO aqueous ink was modified on the flexible PET substrate via inkjet printing, and reduced for use as an electrode²⁷. The ZnO nanorods were then grown, followed by a hydrothermal treatment, as shown in Fig. 1a. The 20-wt% PVDF solution was dissolved in a 1 : 1 mixture of acetone and dimethylformamide (DMF), and was spin-coated onto the ZnO nanorods, which then coagulated²⁸. A poling process was then carried out under a strong constant electric field of 300 kV/cm at 90 °C to induce piezoelectricity and pyroelectricity in the PVDF⁴. A

top electrode of conductive ink was coated onto the PVDF/ZnO nanorod composite film using inkjet printing.

Characterization of the rGO electrode. To fabricate the conductive ink electrode, an aqueous solution GO was synthesized using the Hummers and Offeman method^{29–31}. Fig. 2a shows an atomic force microscopy (AFM) image of the fabricated GO ink, which was a few microns thick, and was composed of 2–3-nm-thick bilayers, as well as some multilayers (>3 nm). To demonstrate the reduction of GO solution to graphene, X-ray photoelectron spectroscopy (XPS) and Raman spectroscopy analysis were carried out. Fig. 2b shows deconvoluted C 1s XPS spectra of the inkjet-printed GO and the reduced GO (rGO) sheets^{18,19}. The C 1s signal of GO has three main components: the C = C and C–C bond vibrations in the aromatic rings (285.0 eV), C–O (286.5 eV) in epoxy or hydroxyl groups, and C = O (288.5 eV) peaks originating from carbonyl and carboxy groups. The ratio I_{C-O}/I_{C-C} decreased from 1.1440 (GO) to 0.2432 (rGO). In addition, a Raman spectrum of the printed rGO sheets on the substrate film is shown in Fig. 2c. The Raman spectra of rGO clearly exhibited the characteristic peaks of the D band ($\sim 1350\text{ cm}^{-1}$), which indicate the typical defects ascribed to structural edge effects, such as epoxides covalently bonded to the base plane, the G band ($\sim 1580\text{ cm}^{-1}$), which indicates a graphite carbon structure, and the ration of I_D/I_G was 0.77^{30,31}.

Characterization of the ZnO nanostructures. The ZnO nanostructures were fabricated using a seed solution zinc acetate ($\text{Zn}(\text{CH}_3\text{COO})_2$) dissolved in ethanol, which was spin-coated onto the rGO-treated PET film. The ZnO nanorods were grown from a mixture of zinc nitrate hexahydrate ($\text{Zn}(\text{NO}_3)_2 \cdot 6\text{H}_2\text{O}$), hexamethylenetetramine and water at 90 °C. The morphology of the ZnO nanorods was controlled by varying the time and concentration of the solution of growth precursor. During the early stages of the hydrothermal method, ZnO nucleates spontaneously from the ionized $\text{Zn}(\text{OH})_4^{2-}$ seed, to form a hexagonal nanostructure in the mixture, which then initiates the growth of one-dimensional (1D) nanorods by increasing the temperature and concentration. As shown in Figs. 3a and b, field-emission scanning electron microscopy (FE-SEM) images reveal that a high density of ZnO nanorods ($1.42 \times 10^{10}\text{ cm}^{-2}$) and disks were formed. Furthermore, high-resolution transmission electron microscopy (HR-TEM) images show that the ZnO nanorods and nanodisks had a well resolved single-crystalline wurtzite structure, with a lattice constant of 0.52 nm in the [0001] growth direction^{32,33}. This indicates that they formed a uniform hexagonal crystal structural without crystalline defects (see inset Fig. 3a and b). The length of the ZnO nanorods was $\sim 300\text{ nm}$, and the diameter was $\sim 85\text{ nm}$; the ZnO nanodisks were $\sim 30\text{ nm}$ in length and $\sim 100\text{ nm}$ in diameter. To investigate the crystal structure of the ZnO nanorods and nanodisks, X-ray diffraction (XRD) analysis was carried out, as shown in Fig. 3c. All of the diffraction peaks could be clearly indexed to the hexagonal ZnO with a lattice constant of $c = 0.5206\text{ nm}$, which is in good agreement with that of ZnO along the c -axis³².

Dielectric properties of the PVDF/ZnO device. The piezoelectric and pyroelectric properties of PVDF are strongly dependent on the β -phase content, owing to large net dipole moment, which originates from the all-trans structure^{4,34}. Therefore, Fourier transform infrared (FTIR) spectroscopy was carried out to investigate the strong dielectric potential, based on the ratio of the α and β phases (I_β/I_α), and the fraction of the β phase, as shown in Fig. 4a. Assuming that the IR absorption follows the Beer-Lambert law, β content in the PVDF can be measured from:

$$F(\beta) = \frac{X_\beta}{X_\alpha + X_\beta} = \frac{A_\beta}{(K_\beta/K_\alpha) + A_\beta} \quad (1)$$

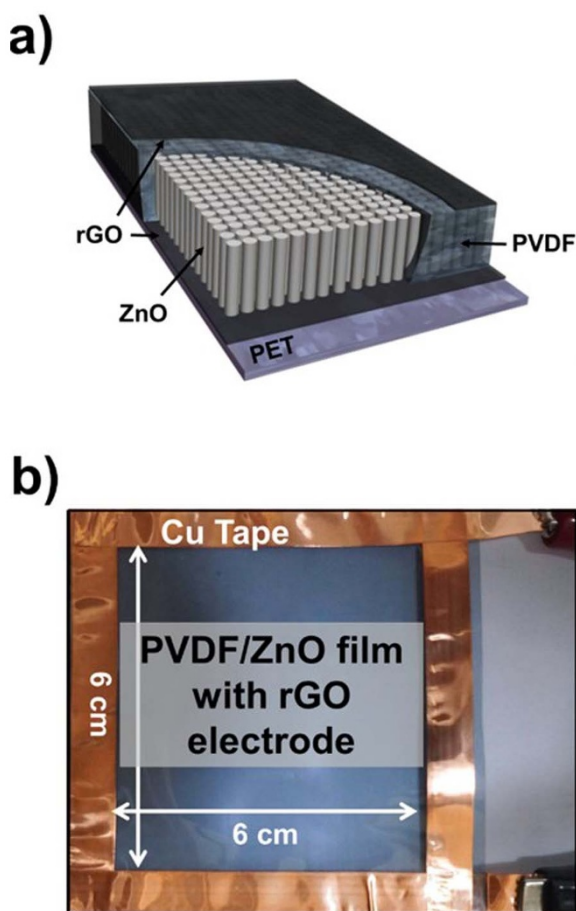


Figure 1 | (a) Schematic diagram and (b) a photograph of the device consisting of the ZnO/PVDF composite film and rGO electrodes.

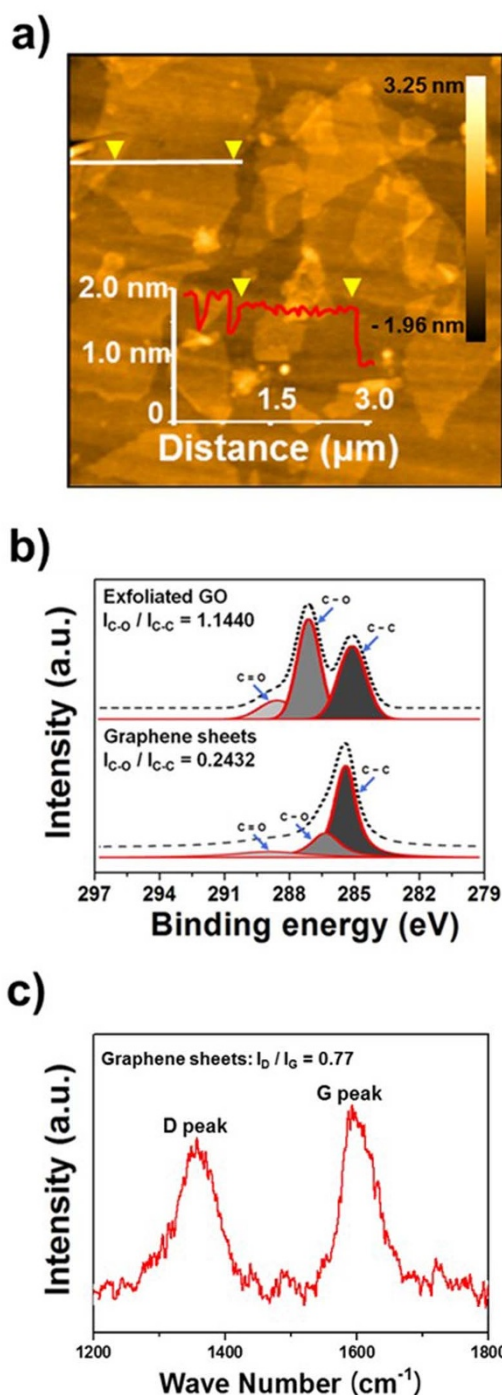


Figure 2 | (a) AFM image of the exfoliated GO solution. (b) XPS spectrum with fitted lines of the pristine and rGO solution for C–C, C–O and C = O bonds. (c) Raman spectra of the rGO electrodes.

where A_α and A_β are the absorbance at 766 and 840 cm^{-1} , respectively, and $K_\alpha = 6.1 \times 10^4 \text{ cm}^2/\text{mol}$ and $K_\beta = 7.7 \times 10^4 \text{ cm}^2/\text{mol}$ are the absorption coefficients of α and β phases at the respective wavenumbers⁴. The PVDF thin film exhibited $I_\beta/I_\alpha = 2.33$, which corresponds to an 85% β phase. (For comparison, commercially available PVDF exhibited $I_\beta/I_\alpha = 1.29$, which corresponds to a 73% β phase content.)

Generally, PVDF with a high β -phase content exhibits enhanced piezoelectric and pyroelectric responses, due to fact that the dipoles are aligned. Also, Fig. S1. shows that observed polarized optical microscopy morphology (POM) of the crystal growth of PVDF with

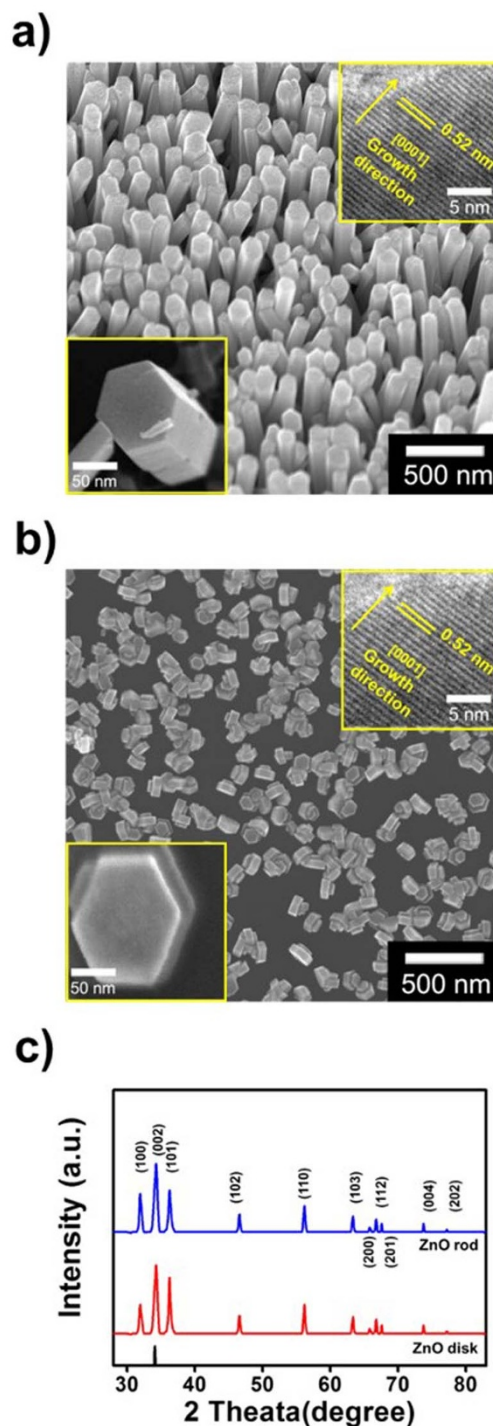


Figure 3 | SEM images of (a) the ZnO nanorods and (b) the ZnO nanodisks. (c) XRD spectra to investigate the crystal structure of the ZnO nanorods and disks.

various ZnO fillers. All samples were isothermally crystallized at 170°C and maintained for 240 s, and it cooled down to observe crystal growth morphology. During poling process of film, high external voltage was applied on the film and polarized ZnO induced β phase of PVDF. Thus, regardless of ZnO morphology, it is clarified that ZnO acts as nuclei for PVDF crystallization. Therefore, we may expect favorable permittivity and losses of sensors fabricated using various ZnO and PVDF thin films. The dielectric properties of PVDF with the embedded ZnO nanorods can be estimated using the Havriliak-Negami and Fourier transfer relationship; i.e.:

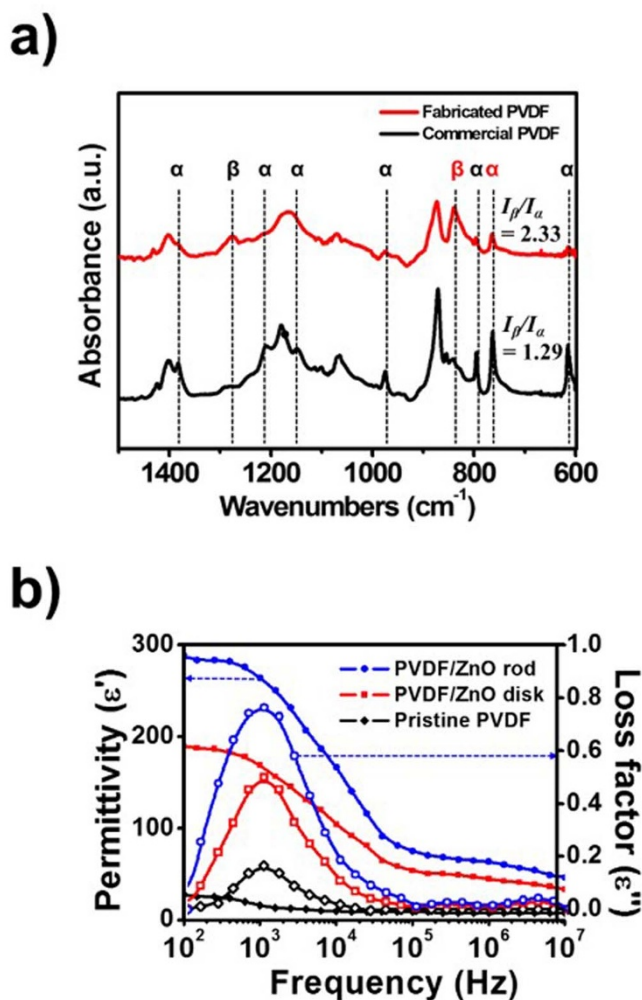


Figure 4 | (a) FTIR spectra of PVDF film fabricated as part of this work, and a commercially available PVDF film. The crystalline phases are indicated. (b) The permittivity and losses of the tactile sensor fabricated with PVDF and different ZnO nanostructures, as well as the PVDF thin film and the commercially available PVDF thin film.

$$\varepsilon^* = \varepsilon' + i\varepsilon'' = \varepsilon_\infty + \frac{\Delta\varepsilon}{1 + (i\omega\lambda)^{1-\alpha}}, \quad (2)$$

Where ε' is the dielectric constant, ε'' is the dielectric loss; the permittivity is therefore given by:

$$\Delta\varepsilon = \varepsilon_s - \varepsilon_\infty \quad (3)$$

where ε_s is the static permittivity (i.e., when $\lim_{\omega \rightarrow 0} \varepsilon^*(\omega)$), and ε_∞ is the high-frequency permittivity (i.e., when $\lim_{\omega \rightarrow \infty} \varepsilon^*(\omega)$)^{4,35,36}.

The measured permittivities of the samples are listed in Fig. 4b. and Table S1. In general the permittivity of a dielectric is larger at lower frequencies than at higher frequencies, and embedding the ZnO in the PVDF significantly increased the dielectric constant. In particular, the ZnO nanorods possessed a greater dielectric constant than the ZnO disks, which is attributable to the larger aspect ratio of the ZnO nanorods, which resulted in a larger energy barrier.

The relaxation time λ is related to the gradient of the loss factor that is associated with the interfacial polarization response of the dielectric material. The relaxation time is given by:

$$\lambda = \frac{1}{2\pi f_{max}}, \quad (4)$$

where f_{max} is the frequency of the peaks in the loss spectrum³⁶. We find a relaxation time of $\lambda = 159$ for the PVDF, $\lambda = 130 \mu\text{s}$ for the ZnO nanodisks, and $\lambda = 121 \mu\text{s}$ for the ZnO nanorods (see Table S1). Based on these dielectric parameters, the inclusion of ZnO in the PVDF film significantly increased the permittivity and reduced the polarization response time of the PVDF-based sensor devices. Since ZnO nanorods with PVDF possessed a higher dielectric constant, the concentration of seed solution was controlled to investigate effects of ZnO rods density. Approximately 30 wt% of zinc acetate dissolved seed solution grow $1.42 \times 10^{10} \text{ cm}^{-2}$, and 25 and 35 wt% represent $0.68 \times 10^{10} \text{ cm}^{-2}$ and $2.54 \times 10^{10} \text{ cm}^{-2}$ of ZnO rods. As a result, 25 wt% of zinc acetate solution sparsely grow ZnO rods compare to 30 wt% of seed solution which result in reduced dielectric properties. Additionally, 35 wt% of seed solution limits dielectric properties of fabricated sample because exceeding density of ZnO rods caused aggregation between rods (Table S2).

Detecting pressure and temperature. To compare the pressure-sensing properties of the PVDF and ZnO/PVDF composite films, pressure stimuli were used, and the performance was measured from the change in the electrical resistance; i.e., $\Delta R = R_{loading} - R_{unloading}$ (Fig. S2). The assembled device had an overlap area of $6 \times 6 \text{ cm}^2$, and was measured with a gradual increase in pressure. Fig. 5a shows how the composite device formed of PVDF, ZnO nanorods and ZnO nanodisks responded to application of a constant pressure. The surface of compressed ZnO nanorods generates a negative potential, and the electrical contact with the rGO electrode layer and the forward bias of the Schottky barrier at the interface results in a change in the resistance of the device (Fig. S3). A difference in the response ΔR to the same pressure was observed between devices, and the PVDF/ZnO nanorod composite device exhibited the greatest signal in response to a given stimulus. Because of the 1D structure of the vertically grown ZnO nanorods, they generate an enhanced piezoelectric response to mechanical displacement than the ZnO nanodisks. The larger aspect ratio and permittivity lead to a change in the electrical resistance in response to even a slight deflection of the ZnO nanorods.

The pressure-sensing capability of the system was evaluated from the response ΔR , as shown in Fig. 5b. The smallest detectable pressure using the ZnO nanorod/PVDF film was 10 Pa (giving $\Delta R = 0.062 \Omega$), which corresponds to 1 mg mm^{-2} , which is 1000-fold more sensitive than the minimum requirements for artificial skin^{3,37–40}. The response times of the output signals from ZnO nanorod/PVDF device were obtained under various pressures at 20°C. The recovery times exhibited similar as shown in Figs. 5c and d. Additionally, three different conducting material of rGO, CNT and PEDOT: PSS were candidate to demonstrate pressure sensitivity as a function of various electrode (Fig. S4.). The sheet resistances of commercial poly(3,4-ethylenedioxythiophene):poly(styrenesulfonate) (PEDOT:PSS) (Sigma-Aldrich) and carbon nanotubes (CNT) (Sigma-Aldrich), and synthesized rGO were 34,10 and 0.7 k Ω /sq. As a result, PVDF/ZnO rods with rGO electrode has highest sensitivity under constant pressure compare to other electrode utilized device.

To investigate the spatial resolution of the pressure-sensing ability, ZnO/PVDF devices were fabricated, as shown in Fig. 6. The film was divided into 144 regions, each $0.5 \times 0.5 \text{ cm}^2$, and Pt weights were used to apply a pressure of 30 Pa at each division, one at a time. The output signal was measured from the change in the resistance using a pseudocolor plot, as shown in Fig. 6a. The two-dimensional (2D) intensity profiles of the ZnO nanorod/PVDF film are shown in Fig. 6b, and the 2D intensity profile of that formed using the ZnO nanodisk/PVDF film are shown in Fig. 6c. The distribution of the operational device area containing the ZnO nanorods in the PVDF thin film was 96%, and that containing the ZnO nanodisks was 77%. As the areal density of ZnO nanorods was larger, and significant

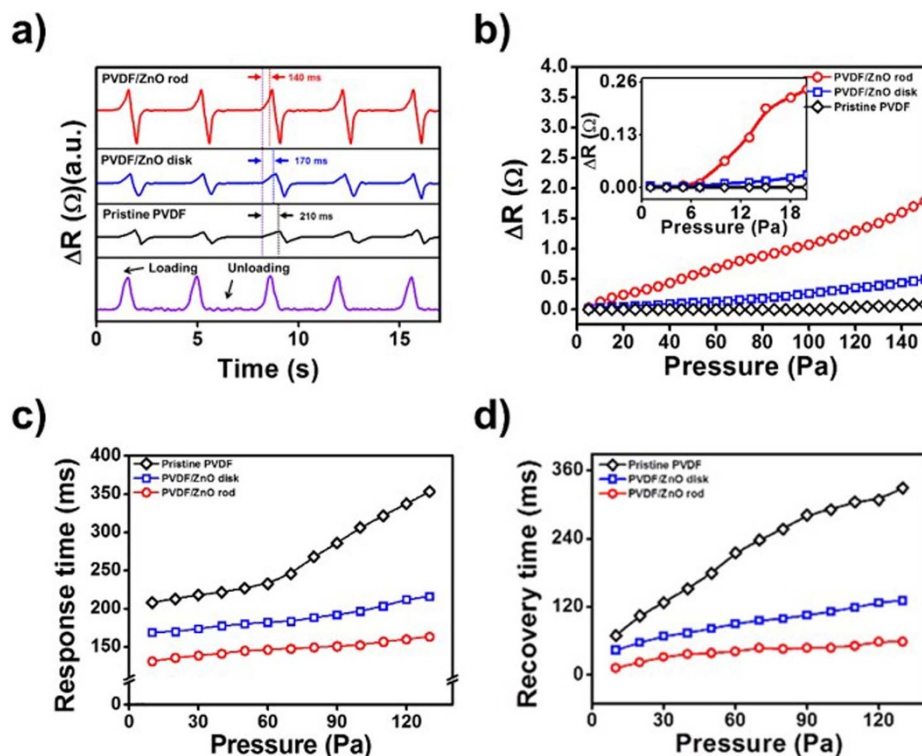


Figure 5 | The change in resistance of the pristine PVDF, and the PVDF/ZnO composite films. (a) In response to an applied pressure of 30 Pa, showing the response time. (b) The sensitivity of the films at 20°C, using various Pt weights. (c) The response and (d) recovery times of the PVDF film, the ZnO nanodisk/PVDF film, and the ZnO nanorod/PVDF with various pressures.

aggregation did not occur, in contrast to the ZnO nanodisks, and so we may expect a more uniform pressure sensitivity with the ZnO nanorod/PVDF composite film.

The device composed of the ZnO nanorod/PVDF composite was used to measure the output signals with various temperatures and applied pressures. To evaluate the pyroelectric response, the Pt weight, which applied a pressure of 30 Pa, were applied at 20, 70, and 120°C in the center of device, as shown in Fig. 7a. We found that the response was slower, and the recovery time longer, at higher temperatures. This is because the pyroelectricity originated from the PVDF, and the thermal energy released from the heated weight on the surface of PVDF thin film resulted in slower motion of the dipoles^{15,34,41–44}. Loading at 20°C resulted in a recovery time of 190 ms, loading at 70°C resulted in a recovery time of 680 ms, and loading at 120°C in a recovery time of 1150 ms.

As shown Figs. 7b and 7c, reproducible responses to changes in temperature and pressure were obtained. The independence of ΔR and the recovery time enabled measurement of pressure and temperature independently. Compare to obtained responses and recovery time, it is found that recovery time has wide delayed time range, 1150 ms at 120°C with 30 Pa whereas delayed response time observes 92 ms. Additionally, the analyzed uniformity of temperature-sensing at the fabricated ZnO nanorods embedded PVDF thin film was 94% (Fig. S5). Considering these results, it is worth nothing that investigation of resistance difference make it feasible to measure the weight of pressure, and delayed recovery time play a pivotal role in determining the temperature of target object.

Application as tactile sensor. Mapping data of the two independent factors was evaluated based on external pressure loaded simultaneously and the temperature of the device. As shown in Figs. 8a and 8b, the applied pressure changed the resistance. Increasing the temperature of the object placed on the then film to apply the pressure increased the recovery time of the signal, and so

the temperature of object could be calculated based on the recovery time. To investigate the scope for simultaneous pressure and temperature sensing in real time, a 15- μ L mineral oil droplet dropped from an initial height of 1.5 cm was measured under a low-noise environment, as shown in Fig. 8c. Data were collected during the initial impact, and during the time when the droplet rebounded from the surface, and impacted again, bouncing on the surface over a period of 1.2 s, as shown in Fig. 8d. The maximum signal at 20°C following the impact of the droplet onto the film was $\Delta R = 1.62 \Omega$, which is equivalent to a pressure of 90 Pa; the recovery time was 180 ms. The signal when a droplet with an unknown temperature was dropped from the same height was monitored. The maximum response was $\Delta R = 1.61 \Omega$. However, recovery time was 815 ms, which corresponds to a droplet temperature of 80°C. The difference in the two peak shapes is attributable to the difference in the sample temperature of each droplet. The 20°C droplet that impacted on the film did not heat the film, because they were at an identical temperature. Therefore, the bouncing movement of a droplet can be detected after its first impact at 510 ms. However, the 80°C droplet was able to transfer both kinetic energy and heat to the film. For this reason, the recovery time was prolonged. Therefore, this system enables independent measurement of pressure and temperature based on the magnitude of the change in the resistance and the recovery time of the signal.

Discussion

We have demonstrated a highly sensitive and multifunctional sensor using a PVDF/ZnO nanorod composite thin film. Existing approaches focus on improving the sensitivity, whereas here we could measure the pressure and temperature independently. The strategy used in the design and fabrication of ZnO nanorods embedded in the PVDF thin film represents a significant advance in the state of the art of nanotechnology fabrication methods. The high sensitivity to pressure and the ability to independently sense temper-

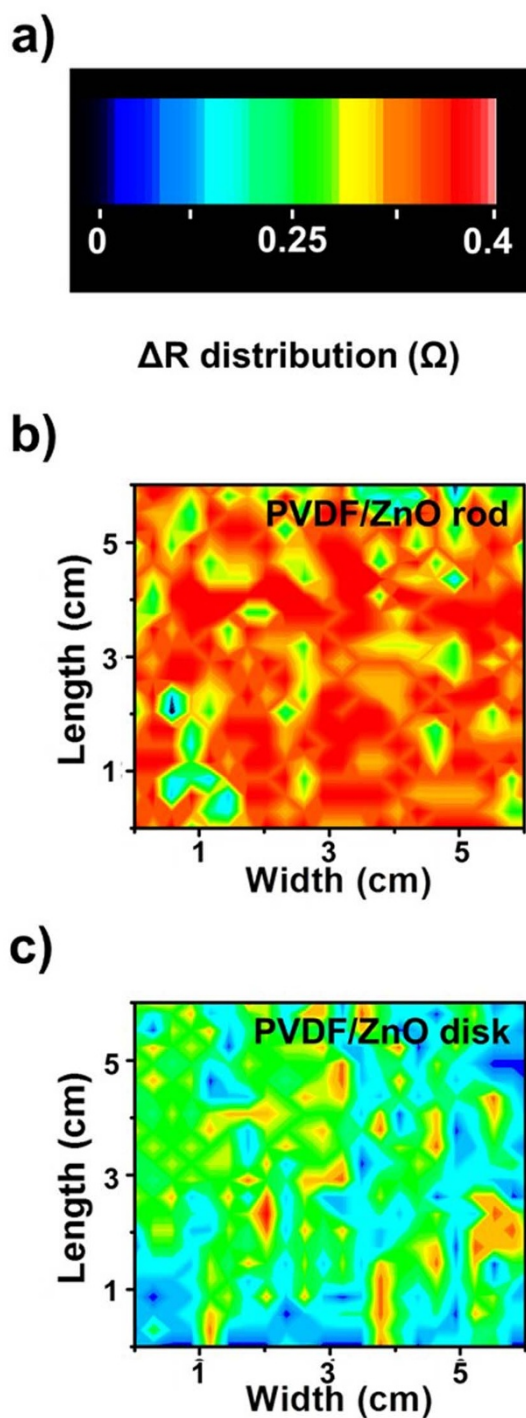


Figure 6 | (a) The spatial variation in the change in resistance. The effective area of fabricated device are $6 \times 6 \text{ cm}^2$. (b) The ZnO nanorod/PVDF film exhibited a higher pressure sensitivity than (c) the ZnO nanodisk/PVDF film. The film was divided into 144 regions ($0.5 \times 0.5 \text{ cm}^2$) and Pt weights were used to apply a pressure of 30 Pa at each division, one at a time.

ature are attributable to the properties of the vertically grown ZnO nanorods and enhanced β -phase component of the PVDF film. The morphology of ZnO nanostructures was either disks or rods (Fig. 3), and could be controlled by varying the process conditions. As a result, the dielectric behavior of PVDF was improved owing to the piezoelectric barrier provided by the ZnO nanorods (Fig. 4).

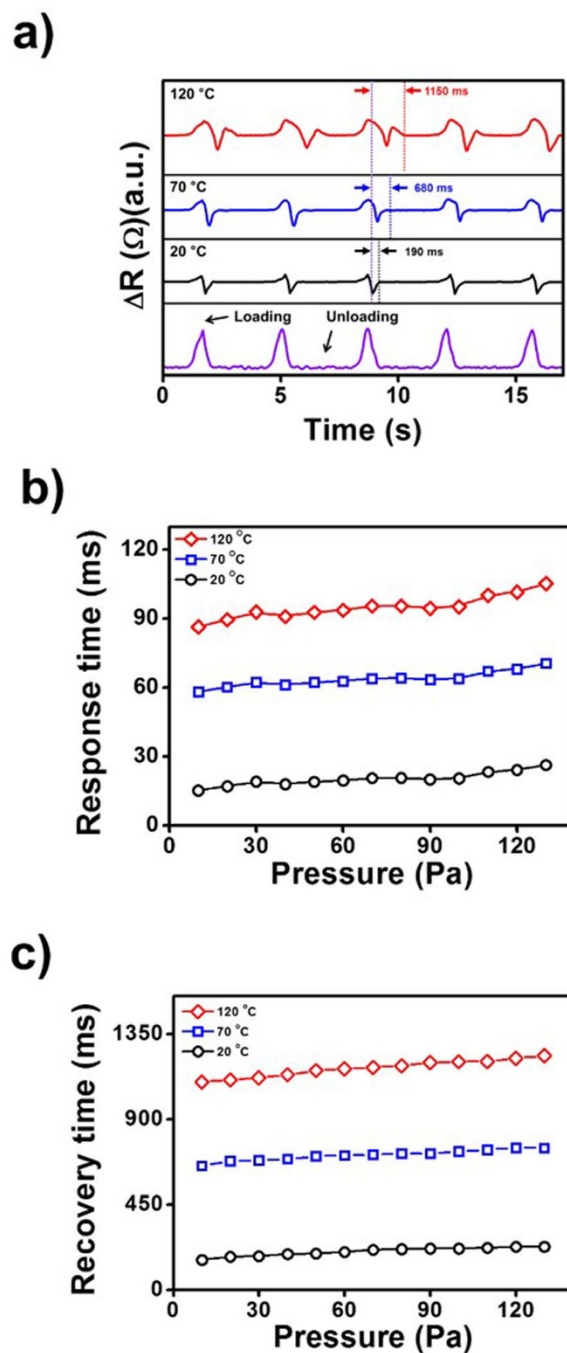


Figure 7 | (a) The output resistance of the PVDF/ZnO nanorod device at various temperatures, 20, 70, and 120 °C, under constant pressure of 30 Pa in the center of device. (b) The response to different pressures and (c) the recovery time at various temperatures.

The composite sensing film exhibited high sensitivity and accuracy, and a real-time response. Using the ZnO nanorods embedded in the PVDF thin film, the pressure sensor could respond to very small pressures, with a minimum detectable pressure of 10 Pa. Moreover, we were able to detect temperatures in the range 20–120 °C. Pyroelectricity induced by the surface of the PVDF film resulted in variation in the output recovery time, from which we could infer the temperature of target object (see Fig. 8).

In conclusion, we fabricated composite ZnO/PVDF thin films, and used these structures to independently measure the pressure applied to the film and the temperature of the object used to apply the pressure. The pressure detection limit was 10^3 -fold lower than the

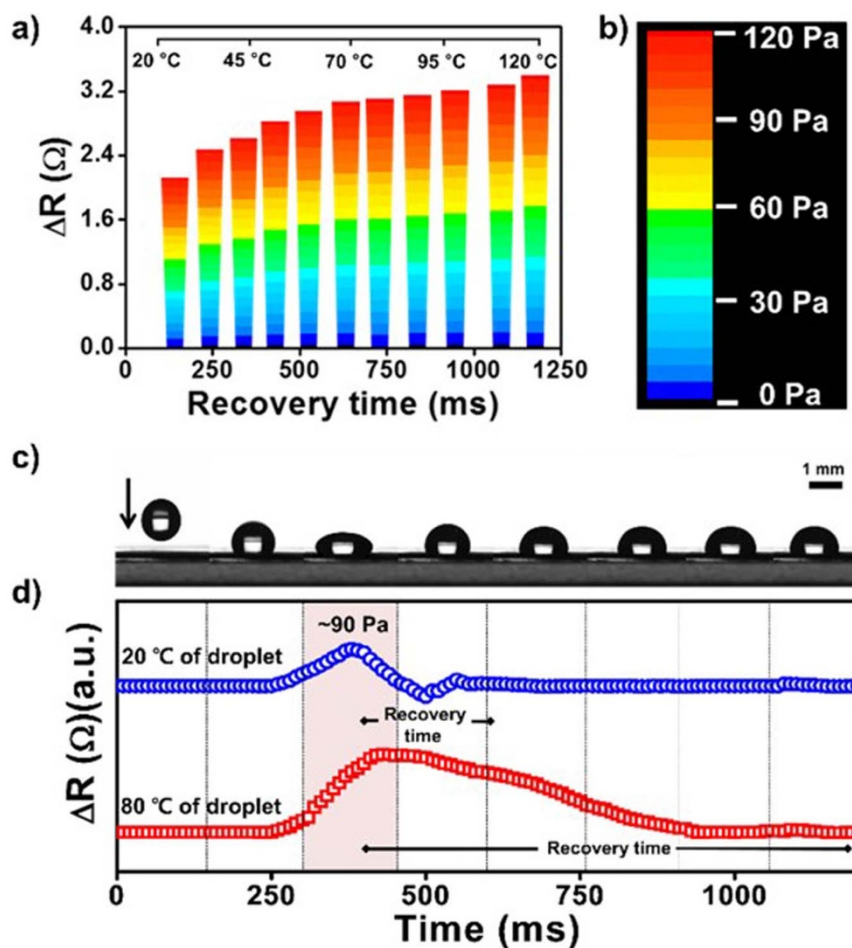


Figure 8 | The relationship between external pressure and the temperature of the object placed on the device to induce a pressure response. (a) The change in the resistance and recovery time. (b) Pseudocolor plots showing the applied pressure on the PVDF/ZnO nanorod film. (c) The response to impact of a droplet with an unknown temperature. (d) The recovery time shows that the temperatures of the droplets were 20°C and 80°C, and the pressure was 90 Pa.

minimum level required for artificial skin, could be monitored in real time, and the temperature could be inferred from the recovery time of the signal. This favorable performance of the e-skin represents a significant advance over the current state of the art, and has potential applications in biorobotic fields.

Methods

Materials. Graphite was purchased from Sigma-Aldrich. The graphene electrodes were printed using a commercially available office inkjet printer (Canon Pixima Ip1300). The polyethylene terephthalate (PET) film, polyvinylidene fluoride (PVDF) pellets (with a molecular weight of 275,000, determined via gel permeation chromatography), zinc acetate dihydrate, zinc nitrate hexahydrate, hexamethylenetetramine and ethanol were obtained from Sigma-Aldrich. PVDF film was obtained from the Fils Corporation (South Korea).

Synthesis of GO dispersion for inkjet printing. GO was synthesized from natural graphite via the modified Hummers and Offeman method, as described by Kovtyukhova and colleagues. Synthesized purified GO suspensions were exfoliated in water by sonication for 1.5 h to avoid blocking the nozzle. The obtained brown dispersion was then washed for 4 cycles of centrifugation at 5,000 rpm to remove any unexfoliated GO.

Modification of the inkjet printer. The ink cartridge (printer head) was disassembled and washed several times using ethanol and distilled water after removing all the inks. The exfoliated GO was dispersed in distilled water at 0.1 wt%, and was injected into the modified cartridge. The sealed ink cartridge was then placed in the printer body for use in further experiments.

Preparation of ZnO. Zinc acetate was dissolved in 100 mL of ethanol, spin-coated onto the rGO-treated PET film, placed in an oven at 100°C, and dried for 30 min

to create a seed layer for subsequent growth of the ZnO nanostructures. A 500-mL solution of 0.05 M hexamethylenetetramine and 0.05 M zinc nitrate hexahydrate and de-ionized water was then coated onto the substrate, and the ZnO nanostructures were grown at 90°C for 3–7 h to control the morphology of ZnO nanostructures.

Preparation of the PVDF thin film. PVDF was dissolved in a 1:1 mixture of DMF and acetone. The solution was stirred at 60°C for 12 h and dropped onto the substrate containing the ZnO nanostructures. Following spin-coating at 1200 rpm for 150 s, the film was poled under an electric field of 300 kV/cm at 90°C.

Characterization. HR-TEM images were captured using a JEOL JEM-3010. Field-emission scanning electron microscopy (FE-SEM) (JEOL JSM-6700F, Japan) and a FTIR spectroscopy (Bomem MB 100, USA) were also used. Atomic force microscopy (AFM) (Nanoscope IIIa, Digital Instruments, USA) was used to image the surface topography. AFM measurements were carried out in tapping mode with silicon tips at a resonance frequency of 320 kHz. The electrical resistance was measured using a Keithley 2400 source meter at 25°C using a four-probe method. Raman spectra were recorded using a LabRAM HR (Horiba, Japan) with 1064-nm laser excitation. For the analysis of detailed force responses, a computer-based user interface and a micro pressure sensor (FT-S270, Nano Science Instrument) with nanoscale-controlled stage by piezoelectric stepping positioner (SLC-1730, Nano Science Instrument) were used to apply an external pressure. Moreover, direction of stepper to apply pressure was vertically loaded and unloaded in order to avoid distortion output signals by torsion or shear stress.

1. Pang, C. *et al.* Flexible and highly sensitive strain-gauge sensor using reversible interlocking of nanofibres. *Nature Mater.* **11**, 795–901 (2012).
2. Pecora, A., Maiolo, L., Maita, F. & Minotti, A. Flexible PVDF-TrFE pyroelectric sensor driven by polysilicon thin film transistor fabricated on ultra-thin polyimide substrate. *Sensor Actuat. A-Phys.* **185**, 39–43 (2012).



3. Hammock, M. L. *et al.* 25th Anniversary Article: The Evolution of Electronic Skin (E-Skin): A Brief History, Design Considerations, and Recent Progress. *Adv. Mater.* **25**, 5997–6038 (2013).
4. Lee, J. S., Shin, K.-Y., Kim, C. & Jang, J. Enhanced frequency response of a highly transparent PVDF–graphene based thin film acoustic actuator. *Chem. Commun.* **49**, 11047–11049 (2013).
5. Kim, D.-H. *et al.* Epidermal Electronics. *Science*. **333**, 838–843 (2011).
6. Moon, H. G. *et al.* Self-activated ultrahigh chemosensitivity of oxide thin film nanostructures for transparent sensors. *Sci. Rep.* **2**, 588 (2012).
7. Mao, S. *et al.* Direct Growth of Vertically-oriented Graphene for Field-Effect Transistor Biosensor. *Sci. Rep.* **3**, 1696 (2013).
8. Yamada, T. *et al.* A stretchable carbon nanotube strain sensor for human-motion detection. *Nature Nanotech.* **27**, 296–301 (2011).
9. Gómez-Martínez, R. *et al.* Silicon chips detect intracellular pressure changes in living cells. *Nature Nanotech.* **8**, 517–521 (2013).
10. Bi, H. *et al.* Ultrahigh humidity sensitivity of graphene oxide. *Sci. Rep.* **3**, 2714 (2013).
11. Ehre, D., Lyahovitskaya, V., Tagantsev, A. & Lubomirsky, I. Amorphous Piezo- and Pyroelectric Phases of BaZrO₃ and SrTiO₃. *Adv. Mater.* **19**, 1515–1517 (2007).
12. Yeo, W.-H. *et al.* Multifunctional Epidermal Electronics Printed Directly Onto the Skin. *Adv. Mater.* **25**, 2773–2778 (2013).
13. Mönch, I. *et al.* Rolled-Up Magnetic Sensor: Nanomembrane Architecture for In-Flow Detection of Magnetic Objects. *ACS Nano*. **9**, 7436–7442 (2011).
14. Calvert, P. Piezoelectric Polyvinylidene Fluoride. *Nature*. **256**, 694 (1975).
15. Lovinger, A. J. Ferroelectric Polymers. *Science*. **220**, 1115–1121 (1983).
16. Kim, J.-H., Beak, J. & Shiv Halasyamani, P. (NH₄)₂Te₃WO₈: A New Polar Oxide with Second-Harmonic Generating, Ferroelectric, and Pyroelectric Properties. *Chem. Mater.* **19**, 5637–5641 (2007).
17. Shin, K.-Y., Hong, J.-Y. & Jang, J. Micropatterning of Graphene Sheets by Inkjet Printing and Its Wideband Dipole-Antenna Application. *Adv. Mater.* **23**, 2113–2118 (2011).
18. Tieke, B. Langmuir-Blodgett Films for Electronic Applications. *Adv. Mater.* **2**, 222–231 (1990).
19. Naciri, J. D. *et al.* Synthesis and Pyroelectric Properties of Novel Ferroelectric Organosiloxane Liquid Crystalline Materials. *Chem. Mater.* **14**, 5134–5139 (2002).
20. Ma, J., Hu, J., Li, Z. & Nan, C.-W. Recent Progress in Multiferroic Magnetolectric Composites: from Bulk to Thin Films. *Adv. Mater.* **23**, 1062–1087 (2011).
21. Cha, S. *et al.* Porous PVDF As Effective Sonic Wave Driven Nanogenerators. *Nano Lett.* **11**, 5142–5147 (2011).
22. Yang, Y. *et al.* Flexible Hybrid Energy Cell for Simultaneously Harvesting Thermal, Mechanical, and Solar Energies. *ACS Nano*. **7**, 785–790 (2013).
23. Hu, W. J. *et al.* Universal Ferroelectric Switching Dynamics of Vinylidene Fluoride-trifluoroethylene Copolymer Films. *Sci. Rep.* **4**, 4772 (2014).
24. Hansen, B. J., Liu, Y., Yang, R. & Wang, Z. L. Hybrid Nanogenerator for Concurrently Harvesting Biomechanical and Biochemical Energy. *ACS Nano*. **7**, 3647–3652 (2010).
25. Omar, K., Ooi, J. & Hassin, M. M. Investigation on Dielectric Constant of Zinc Oxide. *Modern Appl. Sci.* **3**, 110–116 (2009).
26. Ito, D., Jespersen, M. L. & Hutchison, J. E. Selective Growth of Vertical ZnO Nanowire Arrays Using Chemically Anchored Gold Nanoparticles. *ACS Nano*. **2**, 2001–2006 (2008).
27. Shin, K.-Y., Hong, J.-Y. & Jang, J. Flexible and transparent graphene films as acoustic actuator electrodes using inkjet printing. *Chem. Commun.* **47**, 8527–8529 (2011).
28. Choi, S. W., Kim, J. R., Ahn, Y. R., Jo, S. M. & Cairns, E. J. Characterization of Electrospun PVdF Fiber-Based Polymer Electrolytes. *Chem. Mater.* **19**, 104–115 (2007).
29. Kim, K.-H., Lee, K. Y., Seo, J.-S., Kumar, B. & Kim, S.-W. Paper-Based Piezoelectric Nanogenerators with High Thermal Stability. *Small*. **7**, 2577–2580 (2011).
30. Hong, J.-Y. & Jang, J. Micropatterning of graphene sheets: recent advances in techniques and applications. *J. Mater. Chem.* **22**, 8179–8191 (2012).
31. Shin, K.-Y. & Jang, J. Highly conductive, flexible and scalable graphene hybrid thin films with controlled domain size as transparent electrodes. *Chem. Commun.* **50**, 6645–6648 (2014).
32. Panigrahy, B., Aslam, M. & Bahadur, D. Effect of Fe doping concentration on optical and magnetic properties of ZnO nanorods. *Nanotechnology*. **23**, 115601 (2012).
33. Baruah, S. & Dutta, J. Hydrothermal growth of ZnO nanostructures. *Sci. Technol. Adv. Mater.* **10**, 13001 (2009).
34. Chang, D. H. & Yoon, Y. S. Pyroelectric Properties of the B-Polyvinylidene Fluoride (PVDF) Thin Film Prepared by Vacuum Deposition with Electric Field Application. *Jpn. J. Appl. Phys.* **41**, 7234–7238 (2002).
35. Lee, S., Yoon, C.-M., Hong, J.-Y. & Jang, J. Enhanced electrorheological performance of a graphene oxide-wrapped silica rod with a high aspect ratio. *J. Mater. Chem. C*. **2**, 6010–6016 (2014).
36. Hong, J.-Y., Lee, E. & Jang, J. Electro-responsive and dielectric characteristics of graphene sheets decorated with TiO₂ nanorods. *J. Mater. Chem. A*. **1**, 117–121 (2013).
37. Segev-Bar, M., Landman, A., Nir-Shapira, M., Shuster, G. & Haick, H. Tunable Touch Sensor and Combined Sensing Platform: Toward Nanoparticle-based Electronic Skin. *ACS Appl. Mater. Interfaces*. **5**, 5531–5541 (2013).
38. Tee, B. C.-K., Wang, C., Allen, R. & Bao, Z. An electrically and mechanically self-healing composite with pressure- and flexion-sensitive properties for electronic skin applications. *Nature Nanotechnology*. **7**, 825–832 (2012).
39. Van Boven, R. W. & Johnson, K. O. The limit of tactile spatial resolution in humans. *Neurology*. **44**, 2361 (1994).
40. Dellon, E. S., Mourey, R., Dellon, Lee, A. & Dellon. Human Pressure Perception Values for Constant and Moving One- and Two-Point Discrimination. *Plastic & Reconstructive Surgery*. **90**, 112–117 (1992).
41. Lang, S. B. *et al.* Ferroelectric Polarization in Nanocrystalline Hydroxyapatite Thin Films on Silicon. *Sci. Rep.* **3**, 2215 (2013).
42. Jiang, Z. Y., Zheng, G. P., Han, Z., Liu, Y. Z. & Yang, J. H. Enhanced ferroelectric and pyroelectric properties of poly(vinylidene fluoride) with addition of graphene oxides. *J. Appl. Phys.* **115**, 204101 (2014).
43. Chang, H. H. S., Whatmore, R. W. & Huang, Z. Pyroelectric effect enhancement in laminate composites under short circuit condition. *J. Appl. Phys.* **106**, 114110 (2009).
44. Qiu, X. Patterned piezo-, pyro-, and ferroelectricity of poled polymer electrets. *J. Appl. Phys.* **108**, 11101 (2010).

Acknowledgments

This research was supported by the National Research Foundation of Korea (NRF) grant funded by the Korean government (MEST) (Grant no. 2011-0017125).

Author contributions

J.S.L. and K.Y.S. contributed equally to this work; J.S.L., K.Y.S., O.J.C. and J.H.K. designed and performed the experiments, and authored the manuscript; J.S.L. and K.Y.S. contributed to data collection and theoretical analysis; J.J. planned and supervised the project; All authors edited the manuscript.

Additional information

Supplementary information accompanies this paper at <http://www.nature.com/scientificreports>

Competing financial interests: The authors declare no competing financial interests.

How to cite this article: Lee, J.S., Shin, K.-Y., Cheong, O.J., Kim, J.H. & Jang, J. Highly Sensitive and Multifunctional Tactile Sensor Using Free-standing ZnO/PVDF Thin Film with Graphene Electrodes for Pressure and Temperature Monitoring. *Sci. Rep.* **5**, 7887; DOI:10.1038/srep07887 (2015).



This work is licensed under a Creative Commons Attribution 4.0 International License. The images or other third party material in this article are included in the article's Creative Commons license, unless indicated otherwise in the credit line; if the material is not included under the Creative Commons license, users will need to obtain permission from the license holder in order to reproduce the material. To view a copy of this license, visit <http://creativecommons.org/licenses/by/4.0/>